
Article:
Siemiginowska, A. orcid.org/0000-0002-0905-7375, Morganti, R. orcid.org/0000-0002-9482-6844, Fabbiano, G. orcid.org/0000-0002-3554-3318 et al. (4 more authors) (2025) Chandra X-Ray Observatory study of the X-Ray emission of PKS 0023−26 and comparison with recent ALMA results. The Astrophysical Journal, 990 (1). 90. ISSN: 0004-637X

https://doi.org/10.3847/1538-4357/adf19f

The Astrophysical Journal, 990:90 (14pp), 2025 September 1 https://doi.org/10.3847/1538-4357/adf19f

Chandra X-Ray Observatory Study of the X-Ray Emission of PKS 0023−26 and Comparison with Recent ALMA Results

A. Siemiginowska[1], R. Morganti[2,3], G. Fabbiano[1], E. O'Sullivan[1], T. Oosterloo[2,3], C. Tadhunter[4], and D. Burke[1]
[1] Center for Astrophysics | Harvard & Smithsonian, Cambridge, MA 02138, USA; asiemiginowska@cfa.harvard.edu
[2] ASTRON, the Netherlands Institute for Radio Astronomy, Oude Hoogeveensedijk 4, 7991 PD, Dwingeloo, The Netherlands
[3] Kapteyn Astronomical Institute, University of Groningen, Postbus 800, 9700 AV Groningen, The Netherlands
[4] Department of Physics and Astronomy, University of Sheffield, Sheffield S7 3RH, UK
Received 2025 June 6; revised 2025 July 14; accepted 2025 July 16; published 2025 August 29

Abstract

We present a deep high-resolution Chandra X-ray Observatory study of the powerful compact radio source PKS 0023−26 associated with a quasar at redshift 0.322. Earlier studies of the optical environment suggested that the source could be located in a galaxy cluster or a group. However, we report a nondetection of hot gas on large scales (out to ∼60 kpc radius) and place an upper limit on the X-ray luminosity of $<3 \times 10^{42}$ erg s^{-1}, consistent only with the presence of a poor, low-temperature ($kT < 0.5$ keV) galaxy group. X-ray spectral analysis of the central circular region, $r < 7$ kpc, shows, in addition to the mildly absorbed active galactic nucleus, a thermal emission component with a temperature of $kT = 0.9^{+0.19}_{-0.37}$ keV. We discuss the origin of this hot component as a result of interaction between the evolving radio source and the interstellar medium (ISM). Our high-angular-resolution X-ray image traces the distribution of hot gas, which is closely aligned with and extends beyond the radio source, and also in the direction perpendicular to the axis of the radio source. The X-rays are enhanced in the northern radio lobe and at the location of the peak of the CO(3–2)/CO(2–1) line emission, suggesting that the interactions between the jet and cold medium result in the X-ray radiation that excites CO. The shock driven by the jet into the ISM is supersonic with a Mach number of $\mathcal{M} \sim 1.75$–2, creating the cocoon of hot X-rays that surrounds the radio source. This result agrees with observations of shocks in other radio galaxies and points to the prevalent impact of jets on the ISM.

Unified Astronomy Thesaurus concepts: Active galaxies (17); X-ray active galactic nuclei (2035)

1. Introduction

It is well established that relativistic jets emerging from active galactic nuclei (AGNs) are powered by accretion onto supermassive black holes. However, the trigger mechanism of a jet and its connection to the feedback process are not well understood. Recent studies of morphologies (e.g., see C. Ramos Almeida et al. 2011, 2013; J. C. S. Pierce et al. 2022) show strong evidence that the most luminous radio AGNs are triggered by galaxy mergers and interactions. The impact of jets on the interstellar environment may limit the fuel supply and thus regulate black hole activity and its growth (e.g., T. Di Matteo et al. 2005; P. F. Hopkins et al. 2016; D. Mukherjee et al. 2016; S. Cielo et al. 2018).

Radio jets span a broad range of scales, enabling them to influence the surrounding medium from parsecs to hundreds of kiloparsecs. Their large-scale impact is reflected in the morphology of X-ray clusters via large cavities, filaments or shocks (e.g., see reviews by A. C. Fabian 2012; B. R. McNamara & P. E. J. Nulsen 2012). Jets can also drive powerful molecular (R. Morganti et al. 2015; R. Morganti & T. Oosterloo 2018; I. Ruffa & T. A. Davis 2024; and references therein) and warm, emission-line outflows (e.g., C. N. Tadhunter 1991; B. H. C. Emonts et al. 2005; N. P. H. Nesvadba et al. 2006; E. K. Mahony et al. 2016; M. E. Jarvis et al. 2019), which empty the central regions of galaxies and limit the fuel supply to black holes. Observations of nearby X-ray clusters by the Atacama Large Millimeter/submillimeter Array (ALMA) show a rich molecular gas morphology dominated by filamentary or disklike structures, suggesting a relation between the distribution of the cold gas and the jet activity (H. R. Russell et al. 2019). Most of these clusters have well-developed large-scale radio jets and lobes, indicating multiple and ongoing phases of radio activity. Also, in many clusters the X-ray morphology implies that there have been multiple phases of jet activity with timescales as short as a few million years, much shorter than the merger timescales of ∼0.2–1 Gyr derived from cosmological simulations (J. M. Lotz et al. 2011; J. Sabater et al. 2019).

X-ray clusters undisturbed by multiple large-scale radio outbursts, such as those associated with known compact radio sources, are rare. For example, a sample of 46 compact steep-spectrum (CSS) radio sources, which are fully embedded in the ISM of their host galaxy (see C. P. O'Dea 1998; C. P. O'Dea & D. J. Saikia 2021 for a review of the CSS sources), have been observed by Chandra (A. Siemiginowska et al. 2008; M. Kunert-Bajraszewska et al. 2014; M. Sobolewska et al. 2019), and only two CSS sources have been found in bright X-ray clusters (3C 186, $z = 1.06$, A. Siemiginowska et al. 2005, 2010; $1321+045$, $z = 0.312$, M. Kunert-Bajraszewska et al. 2013; E. O'Sullivan et al. 2021). In both cases the small-scale (<10 kpc) CSS radio source is located at the center of a luminous ($L_X > 10^{44}$ erg s^{-1}) cool-core cluster with no detectable signatures of past radio outbursts. Recent studies of two clusters hosting young ($<10^3$ yr) radio galaxies by F. Ubertosi et al. (2023) reveal that the "pre-feedback" clusters exhibit lower central entropy and shorter cooling times than clusters with evolved radio sources.

Table 1
Chandra Observations

Date	Obsid[a]	Exposure[b] (ks)	Net Counts[c]
2021-09-13	24302	27.5	125.3 ± 11.6
2021-09-19	24301	17.6	98.8 ± 10.2
2021-09-20	23839	24.5	128.1 ± 11.6
2021-09-21	26134	28.7	95.0 ± 10.1
2021-09-23	24300	32.6	130.5 ± 11.7
2021-09-24	24303	29.0	129.4 ± 11.7

Notes.
[a] Chandra obsid.
[b] Effective exposure time for each obsid.
[c] Number of background-subtracted counts in the 0.5–7 keV energy range in an $r = 1\farcs5$ circular region centered on the source.

Observations of warm ionized gas or the cold molecular component show that young radio jets can drive fast outflows and increase the turbulence of the surrounding gas (e.g., J. Holt et al. 2003, 2008; P. Guillard et al. 2012; C. Tadhunter et al. 2014; C. M. Harrison et al. 2018; F. Santoro et al. 2020; G. Cresci et al. 2023; J. H. Costa-Souza et al. 2024; I. Ruffa & T. A. Davis 2024). The powerful jets can shock the ISM, resulting in aligned X-ray radiation, as observed in nearby radio galaxies (e.g., in 3C 171, M. J. Hardcastle et al. 2010; 3C 305, F. Massaro et al. 2009; M. J. Hardcastle et al. 2012; PKS B2152-69, D. M. Worrall et al. 2012; 3C 303.1, C. P. O'Dea et al. 2006; F. Massaro et al. 2010; 3C 237, F. Massaro et al. 2015; and CSS sources, C. P. O'Dea et al. 2017).

Additionally, theoretical models predict that the lobes of small-scale radio sources can emit relatively strong X-rays via inverse Compton scattering on the hot relativistic plasma (Ł. Stawarz et al. 2008; D. Ł. Król et al. 2024). Chandra observations have shown that jets interact with the ISM of the host galaxy, causing either shock ionization (e.g., J. Wang et al. 2011 in NGC 4151; A. Paggi et al. 2012 in MRK 573) or compression, resulting in enhanced, cooler X-ray emission (G. Fabbiano et al. 2022 in NGC 6117). Embedded jets in ISM-rich galaxy disks may also cause lateral outflows and hot X-ray halos (D. Mukherjee et al. 2016, 2018) that have been detected in nearby AGNs with Chandra and the Hubble Space Telescope (e.g., in ESO 428-G014, G. Fabbiano et al. 2018; in IC 5063, W. P. Maksym et al. 2020; A. Travascio et al. 2021; and in NGC 6117, G. Fabbiano et al. 2022; see also the review by G. Fabbiano & M. Elvis 2022).

In order to study the impact of a young radio source on the ISM of its host galaxy, and also to connect to the larger-scale environment, we obtained a deep Chandra observation of PKS 0023−26, a double-lobed CSS radio source at redshift $z = 0.32188(4)$ (F. Santoro et al. 2020) with a size of ∼3 kpc (peak-to-peak lobes; a full extent up to ∼4.7 kpc; A. Tzioumis et al. 2002) and a radio core detected in recent ALMA observations (R. Morganti et al. 2021). The powerful radio source ($\log(P_{5\,\mathrm{GHz}}/\mathrm{W\,Hz^{-1}}) = 27.43$) is hosted by an early-type galaxy (C. Ramos Almeida et al. 2011) and it is classified as a Type 2 quasar with a bolometric luminosity in the range $(2.5–4) \times 10^{45}\,\mathrm{erg\,s^{-1}}$ (J. Holt et al. 2008; F. Santoro et al. 2020).

There are several early-type galaxies located $<30''$ away from PKS 0023−26, including three galaxies at similar redshift located in projection at distances of $5\farcs8$ (27 kpc), $6\farcs9$ (32.5 kpc), and $25\farcs8$ (116 kpc), suggesting that PKS 0023−26 could be located at the heart of a rich cluster of galaxies (C. Tadhunter et al. 2011; C. Ramos Almeida et al. 2013). On the other hand, based on short XMM-Newton observations, the total X-ray luminosity of PKS 0023−26 and its surroundings ($\log(L_{2-10\,\mathrm{keV}}/\mathrm{erg\,s^{-1}}) = 43.27$; B. Mingo et al. 2014) is lower than expected for a rich cluster of galaxies, and is more consistent with that of a galaxy group (H. J. Eckmiller et al. 2011). The questions about the environment of PKS 0023−26 and the impact of the radio source on the ISM have motivated the new Chandra X-ray observations presented in this paper.

Recent ALMA studies of this quasar (R. Morganti et al. 2021; T. Oosterloo et al. 2025, hereafter Paper I) provide a comprehensive characterization of the cold molecular gas. Together with the Chandra results, we can now compile a multiphase picture of the environment of PKS 0023−26.

We obtained a deep Chandra observation of PKS 0023−26 and aimed to detect the X-ray gas associated with a group or cluster, evaluate the X-ray morphology of the hot gas on subarcsecond scales, and study the distribution of the hot gas in relation to the molecular gas. Our goal was also to study the spectral properties of the central AGN and the impact of a young radio jet on the ISM on smaller radial scales. We did not detect an X-ray-luminous cluster, but we found hot gas surrounding the radio source, indicating interactions between an evolving jet and the ISM. We present the Chandra observations and data analysis in Section 2, describe the results in Section 3, and in Section 4 we discuss our results in the light of the radio and molecular ISM properties.

We adopted the flat Universe cosmology with $H_0 = 70\,\mathrm{km\,s^{-1}\,Mpc^{-1}}$, $\Omega_\Lambda = 0.7$, and $\Omega_\mathrm{M} = 0.3$ (G. Hinshaw et al. 2013); $1''$ corresponds to 4.716 kpc at the $z = 0.322$ redshift of PKS 0023−26.

2. Chandra Observations and Data Analysis

The Chandra observation of PKS 0023−26 was performed in 2021 September with the Advanced CCD Imaging Spectrometer (ACIS-S) and the readout of the full CCD in the VFAINT mode. The source was placed on the S3 chip at the nominal aim-point for the Cycle 22 observations. The total exposure time of ∼160 ks was split into six separate pointings with exposure times from 17.6 to 32.6 ks. We list information about each pointing in Table 1, including the obsid, effective exposure time, and measured source counts.

We used CIAO v.4.16 (A. Fruscione et al. 2006) and the calibration CALDB v.11.2 for the X-ray data analysis.

2.1. Image Analysis

The deep Chandra observation of PKS 0023−26 was split into six individual pointings, carried out over the course of 10 days (see Appendix A, which shows individual observations). The source flux did not vary during that time within the 90% measurement uncertainties (see Table 4 in Appendix A). We applied the astrometric correction with `wcs_match`, `wcs_update`, and `reproject_events` tools to each data set before merging the six event files with `dmmerge`. The merging of these observations resulted in a deep X-ray image with a total exposure time of 160 ks, shown in Figure 1, which provides the highest S/N to search for possible diffuse emission surrounding PKS 0023−26.

Chandra X-ray images have the highest angular resolution attainable to date and, depending on the observation setting,

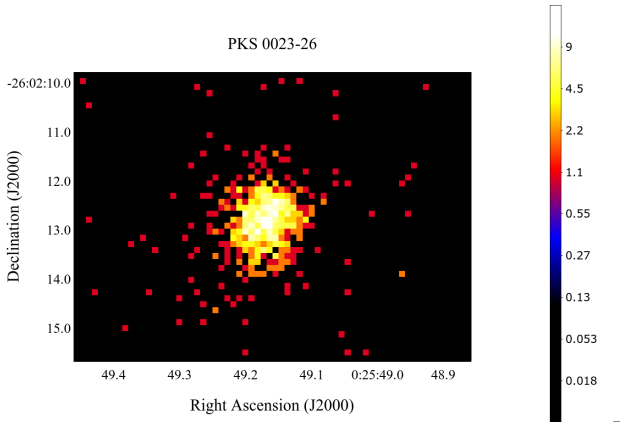

Figure 1. Chandra ACIS-S image of PKS 0023−26 in the 0.3–7 keV energy range. The X-ray image is binned to 1/4th ACIS pixel size (0.″123). The scale is logarithmic and the color indicates counts in a pixel as shown on the bar to the right.

they can achieve a subpixel resolution, i.e., <0.″492 for the ACIS-S detector. In our analysis we used `chandra_repro` and applied the EDSER repositioning algorithm (`pix_adj=EDSER`, J. Li et al. 2004), which improves the photon localizations and results in a 40%–70% narrower default point-spread function (PSF). This allows for the analysis of on-axis images at the bin size of 0.″0615 (see, e.g., J. Wang et al. 2011). However, the angular image resolution depends on the shape of the PSF[5] at a given off-axis location of the source. Thus we perform the PSF simulations (see Section 2.1.1 below) to evaluate the angular resolution of the X-ray images we discuss in the following sections.

Figure 2 shows two X-ray images of PKS 0023−26 with the counts accumulated in the soft (0.3–2 keV) and hard (2–7 keV) energy ranges respectively. The images are binned to 0.″123 pixel size. The hard image has a more defined core emission and some scatter around it. The soft image shows a more uniform distribution of counts with no specific core visible. Such a difference in morphology is expected for an absorbed AGN—the core visible in the hard band and absorbed in the soft band, with the soft X-rays originating outside the primary core region. We will perform the spectral analysis to quantify the parameters of the X-ray radiation (see Section 3.3).

2.1.1. PSF Simulations

The peaked PSF is energy-dependent and contains about 50% of counts within a compact radius of about <0.″25 at soft energies <1.5 keV (on-axis).[6] However, the shape of the Chandra PSF varies widely across the field of view and it cannot be described analytically, therefore high-resolution image analysis requires the PSF simulation with CIAO tools, CHART and MARX. We input the best-fit spectrum, the source coordinates for each observation, and the aspect solution files to CHART and generated 50 random PSF rays, which were projected onto the ACIS-S detector using MARX (with the corresponding aspect dither and specific coordinates for each observation RA_NOM, DEC_NOM, ROLL_NOM) and merged into one PSF for a specific `obsid`. We added an intrinsic broadening of the PSF using the BLURR parameter in MARX set to 0.″07 (see J. Ma et al. 2023 for a discussion on the Chandra PSF). We generated the final PSF by merging the PSFs simulated for each `obsid`.

[5] https://cxc.cfa.harvard.edu/ciao/PSFs/psf_central.html

[6] Chandra Observatory Guide:https://cxc.harvard.edu/proposer/POG/html.

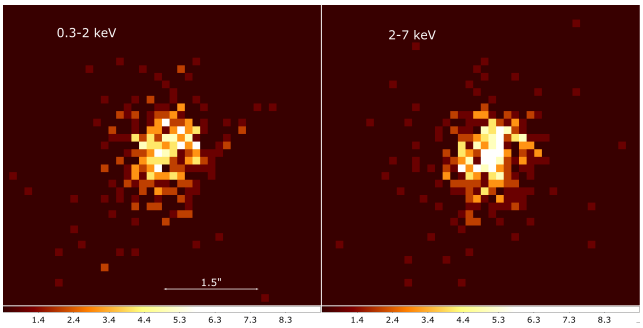

Figure 2. Chandra ACIS-S image of PKS 0023−26 in two energy bands: soft (0.3–2 keV, left) and hard (2–7 keV, right). The X-ray image is binned to 1/4th ACIS pixel size (0.″123). The arrow shows the 1.″5 scale and the size of each image is 5.″9 × 5.″9. The color indicates counts in a pixel as shown on the color bars.

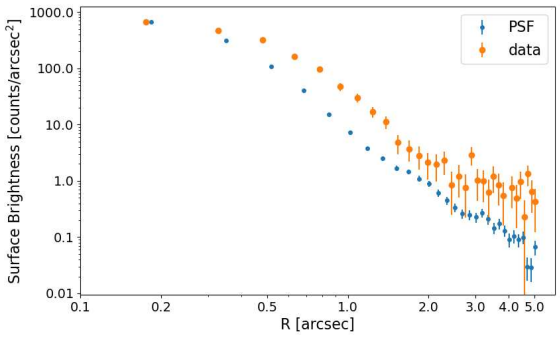

Figure 3. Surface brightness profiles of the PKS 0023−26 X-ray image (0.5–7 keV, in orange) and the Chandra PSF (in blue).

We extracted the surface brightness profiles of the X-ray emission and the PSF assuming annular regions centered on the peak emission. The observed surface brightness profile of PKS 0023−26 is broader than the PSF at scales larger than >0.″32, and thus not consistent with point-source emission (see Figure 3). Note that this is also a rough estimate of the angular resolution of the images we discuss in Section 3.2.

2.2. Spectral Analysis

We used `specextract` in CIAO to obtain the X-ray spectrum of PKS 0023−26 in each individual observation, assuming a circular region with $r = 1.''5$ (∼7 kpc, PSF fraction of 94%) radius centered on the source. The background spectra were extracted from an annulus centered on the source with inner and outer radii of 2.″8 and 5.″8 respectively. The associated response files and effective area files were generated for each observation. The six spectra and the responses were combined into one spectrum using the `combine_spectra` script, resulting in a total of 692.3 ± 26.5 net counts. We model this spectrum in Sherpa (P. Freeman et al. 2001; A. Siemiginowska et al. 2024) using the fit statistic `cstat` based on the Poisson likelihood (see Sherpa documentation for details).

The spectral extraction region, $r = 1.''5$, includes the emission of the AGN, an intrinsic absorption associated with the nucleus/core, radiation scattered off the molecular medium in the nucleus/core, and the addition of diffuse emission on larger scales but still within <1.″5 (<7 kpc) from the nucleus.

Table 2
Best-fit X-Ray Model Parameters for the Central $r \leqslant 1.''5$ Region

Model	$N_{\rm H}(z)$	Γ	Line (E) or Line (z)	EW (keV)	T (keV)	$f_{0.5-7.0\,\rm keV}$ [a]	Stat./dof
phabs*zphabs*pow	<4.0	$1.23^{+0.15}_{-0.12}$	…	…	…	7.5 ± 0.6	475.8/443
phabs*zphabs*(pow+zgauss)	<4.7	$1.32^{+0.19}_{-0.13}$	6.32 ± 0.07	$0.34^{+0.16}_{-0.03}$	…	$7.6^{+0.7}_{-0.9}$	458.6/441
phabs*zphabs*(pow+zgauss)*	<4.9	$1.31^{+0.17}_{-0.13}$	0.339 ± 0.014	$0.37^{+0.01}_{-0.05}$	…	7.5 ± 0.7	458.6/441
phabs*(zphabs*(pow+zgauss)+apec)	$6.1^{+6.4}_{-5.2}$	$1.45^{+0.27}_{-0.25}$	6.32 ± 0.05	$0.335^{+0.11}_{-0.06}$	$0.91^{+0.25}_{-0.34}$	8.86 ± 0.03	449.2/439
phabs*(zphabs*(pow+zgauss)+apec)*	$6.1^{+6.4}_{-5.2}$	1.45 ± 0.25	0.339 ± 0.010	$0.331^{+0.111}_{-0.096}$	$0.91^{+0.23}_{-0.33}$	9.38 ±1.1	449.2/439

Note. Galactic absorption (phabs model) of $N_{\rm H} = 1.82 \times 10^{20}\,{\rm cm}^{-2}$ included in all models; $N_{\rm H}(z)$—intrinsic absorption (zphabs model) is given in units of $10^{21}\,{\rm cm}^{-2}$; redshift $z = 0.322$ is frozen for the intrinsic absorption and the thermal model (apec). *—line energy is frozen at 6.4 keV (zgauss model); equivalent width (EW) and temperature are given in units of keV. The abundances parameter is set to 1 in the apec model. Uncertainties are 90%. The last column lists Cstat statistics and degrees of freedom for the best-fit model.
[a] Observed corrected for absorption flux in units of $10^{-14}\,{\rm erg\,cm^{-2}\,s^{-1}}$.

An AGN X-ray spectrum associated with the accretion flow and the hot corona is characterized by a power law. This radiation could be absorbed by a large amount of gas, and it can also be scattered off the molecular medium, resulting in the narrow iron line, Fe Kα, emitted at $E = 6.4$ keV (see review by R. C. Hickox & D. M. Alexander 2018). We applied several models with increasing complexity and number of parameters to the combined X-ray spectrum of PKS 0023−26. The models defined in Sherpa were used to build model expressions: (1) A simple power law model, `powlaw1d`, defined on energy scale E, $M(E) = {\rm Norm} \times E^{-\Gamma}$ with the normalization at 1 keV in units of [photons cm^{-2} s^{-1}] and a photon index Γ; (2) The Galactic absorption model, `phabs`, a multiplicative expression $\exp[-N_{\rm H}\sigma_E]$ with the equivalent hydrogen column $N_{\rm H}$, and the atomic cross sections σ_E from E. Anders & N. Grevesse (1989); (3) The intrinsic absorption, `zphabs`, at the redshift of the source: $\exp[-N_{\rm H}(z)\,\sigma_{E[1+z]}]$; (4) A redshifted Gaussian line, `zgauss`, to account for Fe Kα emission, with the parameters describing the redshift, the energy of the line location, the line width, and the normalization defined as the total number of photons in the line in units of [photons cm^{-2} s^{-1}]; (5) An `apec` model describing emission from a collisionally ionized plasma at a given temperature (in keV units), calculated from the AtomDB[7] atomic database (A. R. Foster et al. 2012), at the source redshift and assumed metallicity in terms of the solar abundances.

We performed simulations to assess the significance of including the emission line and a thermal component using the `plot_pvalue` function in Sherpa (R. Protassov et al. 2002). Additionally, we ran the Metropolis–Hastings Bayesian Markov Chain Monte Carlo (MCMC) sampler with the `get_draws` function, assuming default flat priors and 5×10^4 iterations, to evaluate the posterior probability distributions for the complex models. We utilized the `corner` Python package (D. Foreman-Mackey 2016) to visualize these distributions (see Appendix A).

We list the best-fit model parameters for the X-ray spectrum of PKS 0023−26 in Table 2 and present the results in Section 3.

3. Results

3.1. X-Ray sources

The centroid of the X-ray source PKS 0023−26 is located at R.A., decl. (J2000) = $0^{\rm h}25^{\rm m}49\overset{\rm s}{.}24$, $-26^\circ02'12\overset{\prime\prime}{.}6$ with $0\overset{\prime\prime}{.}05$ uncertainty. PKS 0023−26 X-ray emission is not consistent with the emission of a point source. Figure 3 shows a surface brightness profile of PKS 0023−26 with an excess X-ray emission over the PSF profile at radii $\sim 0\overset{\prime\prime}{.}4$–$5''$. There is no indication of an extended, X-ray diffuse emission surrounding the source on larger scales. We estimate the limit on the X-ray diffuse emission below in Section 3.3.

We also detect a second X-ray source at R.A., decl. (J2000) = $0^{\rm h}25^{\rm m}50\overset{\rm s}{.}56$, $-26^\circ02'14\overset{\prime\prime}{.}7$, about $18''$ to the east of PKS 0023−26 (see Figure 13). The source is present in the Gaia DR2 (Gaia Collaboration et al. 2018) optical catalog with ID = 2323489174407213824 and an average G magnitude of 20.6525 ± 0.0211. We discuss the X-ray properties of this source in Appendix B.

3.2. Distribution of the Hot Gas

We focus our analysis on the morphology of the hot gas in the central regions, within <10 kpc of the source. In order to characterize the shape and size of the X-ray emission we fit the broadband X-ray image of PKS 0023−26 in Sherpa assuming a 2D Gaussian model convolved with the PSF. This model accounts for the AGN point-source emission expected to follow the PSF shape and an additional smooth structure modeled as a Gaussian. Figure 4 shows the data, model, residual, and PSF images (see Appendix A for parameters distributions from MCMC sampling) The residual image shows an elongated emission in the direction consistent with the radio source. Accounting for the ellipticity and rotation using the `sigmagauss2d` model we obtained the deconvolved 1σ width equal to $\sigma_{\rm maj} = 0\overset{\prime\prime}{.}36 \pm 0\overset{\prime\prime}{.}02$ and $\sigma_{\rm min} = 0\overset{\prime\prime}{.}24 \pm 0\overset{\prime\prime}{.}02$. We note that this scale agrees with the distance between the peaks of the radio lobes of $0\overset{\prime\prime}{.}62$ and may relate to the hot "cocoon" emission surrounding the radio source. In this model there is still an excess of the X-ray emission toward the northern lobe, indicating additional enhancement possibly related to the jet–clouds interactions, which we discuss in Section 4.3.

We generated the high-resolution images for the broad (0.3–7 keV), soft (0.3–3 keV), and hard (3–7 keV) bands by binning the merged event file into the 1/16th ACIS pixel size images, which were adaptively smoothed with `dmimgadapt` using Gaussian kernels ranging from 0.5 to 10 pixels (30 iterations and assuming five counts under the kernel). Figure 5 shows the resulting smoothed images overlaid with the radio source contours. The X-ray emission is elongated, follows the direction of the radio source shown in contours, and has a

[7] http://atomdb.org/

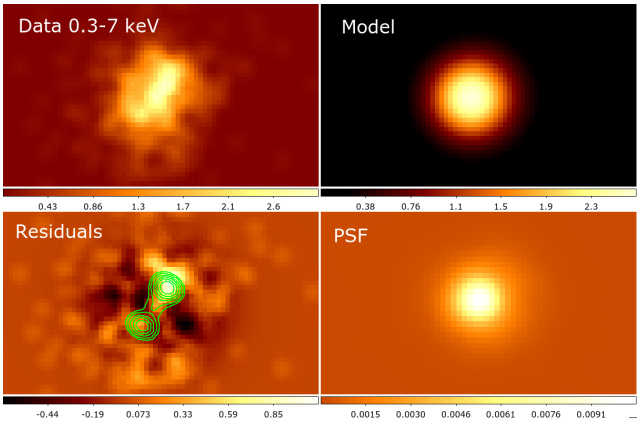

Figure 4. 2D model fit to the broad X-ray image of PKS 0023−26. Four panels show the X-ray image (upper left), best-fit image of a 2D Gaussian circular model (upper right), the residuals (lower left), and the Chandra PSF image normalized to 1 (lower right). The color bars show intensity levels. The data and residual images were smoothed with a Gaussian with $\sigma = 3$ pixels and pixel size equal to 0.″123. The image of the residuals is overlaid with the 87 GHz radio continuum contours with levels (1, 2.3, 5.6, 11, 19, 33) mJy beam^{-1} (beam = 0.″163 × 0.″09474).

spatial scale similar to the radio source. The soft-band image shows a clumpy structure and enhanced emission at the location of the radio lobes. It is also slightly offset from the position of the radio core. The hard-band X-ray radiation is more concentrated in the core region.

We further investigate the differences between soft and hard X-ray morphology using the map of hardness ratio (X-ray color) defined as (H − S)/(H + S), where H = 2–7 keV image and S = 0.3–2 keV image. The resulting hardness ratio images are shown in Figure 6 together with the radio source contours. The harder X-ray emission surrounds the southern lobe and the western side of the radio source, although the overall radiation enclosing the radio source is relatively hard (green and blue colors in the maps). Our spectral modeling of the X-ray emission in the smaller subregions also implies a difference between the southern and northern subregions, which we describe in Section 3.4.

3.3. Spectral Analysis and Results

We list the best-fit parameters for the models applied to the X-ray spectrum of PKS 0023−26 in Table 2.[8] The best-fit photon index of the power-law models is relatively "hard," between $1.23^{+0.15}_{-0.12}$ in the simplest model and 1.45 ± 0.25 in the most complex one. We detect the Fe Kα emission line (p-value < 0.0002), located at the rest-frame energy of $E_{\rm rest} = 6.34 \pm 0.07$ keV with an equivalent width of $0.34^{+0.16}_{-0.03}$ keV, consistent with reflection from the cold medium (e.g., Y. Fukazawa et al. 2011). Figure 7 shows the absorbed power-law model and Fe Kα emission line fit to the X-ray spectrum of PKS 0023−26.

The most complex models (4 and 5 in Table 2) include thermal emission from a collisionally ionized medium (apec) potentially associated with the jet-heated ISM (see, e.g., G. Fabbiano et al. 2019b). These are the most likely models for the X-ray spectrum of PKS 0023−26. The MCMC sampling results show relatively broad parameter distributions and the potential presence of a low-temperature component (see Appendix A). However, we are unable to evaluate the two-temperature model with the current data. The apec model with a plasma temperature of $kT = 0.91^{+0.19}_{-0.37}$ keV (1σ) is present in the X-ray spectrum (p-value < 0.0002) with the observed (0.5–2 keV) flux equal to $(1.1 \pm 0.3) \times 10^{-14}$ erg cm^{-2} s^{-1}, corresponding to a hot-medium luminosity of $L_{(0.5-2\ {\rm keV})} = (3.82 \pm 0.34) \times 10^{42}$ erg s^{-1}.

The flux of the power-law model, corrected for absorption, in the 0.5–7 keV energy band is equal to $(7.5 \pm 0.6) \times 10^{-14}$ erg cm^{-2} s^{-1}, which corresponds to a luminosity of 2.6×10^{43} erg s^{-1}. We measure a luminosity of 3.1×10^{43} erg s^{-1} in the 2–10 keV band, similar to the X-ray luminosity derived from XMM observations (B. Mingo et al. 2014). We note that the XMM 30″ source extraction region contained the second X-ray source located 18″ away that was resolved in Chandra observations. However, this second source should not contribute to the XMM (2–10 keV) luminosity as it has a softer spectrum and it is fainter than PKS 0023−26 in this energy band ($\Gamma = 2.33^{+0.19}_{-0.28}$, $f^{\rm cont}_{(2-10\ {\rm keV})} = 1.04^{+0.24}_{-0.17} \times 10^{-14}$ erg cm^{-2} s^{-1}, see Appendix B).

We do not detect thermal emission on a large scale outside the central region of PKS 0023−26. However, we can estimate the limit on this emission by modeling the X-ray spectrum from an $r \leqslant 12''$ circle, excluding the central $r = 1.''5$. For an absorbed power law with $\Gamma = 1.45$ plus apec model with $kT = 0.5$ keV we obtained a 90% limit on the flux of the apec model of $f^{\rm apec}_{(0.5-2\ {\rm keV})} < 9.5 \times 10^{-15}$ erg cm^{-2} s^{-1}, corresponding to a thermal luminosity of $< 3.2 \times 10^{42}$ erg s^{-1}. For the higher temperature, $kT = 1$ keV, the limit is $f^{\rm apec}_{(0.5-2\ {\rm keV})} < 4.9 \times 10^{-15}$ erg cm^{-2} s^{-1}, corresponding to a luminosity of $< 1.7 \times 10^{42}$ erg s^{-1}. We note that this limit on the large-scale luminosity implies that the central X-ray emission cannot be associated with a cool core of a rich galaxy cluster (see discussion in Section 4.1).

To summarize, our spectral analysis indicates the presence of thermal emission contributing to the central X-ray spectrum of PKS 0023−26, and we are able to place a limit on the thermal emission on a large scale. The primary AGN emission is absorbed and also reflected off the cold medium as revealed by the Fe Kα emission line. The elongated shape of the X-ray spectrum closely aligned with the radio source indicates a jet–ISM connection and possibly suggests jet heating. We will take this into account in the discussion in Section 4.3.

3.4. Spectral Analysis of Sectors

We split the X-ray image of the circle of radius 1.″5 into four 90° sectors, and obtained spectra for each sector (pie region in CIAO). Figure 8 shows the regions with the corresponding number of X-ray counts at 0.3–7 keV. Higher numbers of counts are detected in regions 1 and 3, which also correspond to the north and south directions of the radio lobes.

We applied an absorbed power-law model plus a Gaussian emission line to the spectrum of each sector. We also applied an absorbed apec plasma model to each sector; however, we are unable to obtain valid solutions with the low counts spectra in these sectors. We list the best-fit model parameters in Table 3. The two sectors to the north, 1 and 2, show intrinsic absorption with an equivalent column density of about (5–6) × 10^{21} cm^{-2}, but with large uncertainties (upper bound in each case). There is no detectable absorption in the other

[8] Note that the X-ray spectrum was extracted from a circular region with $r = 1.''5$ radius.

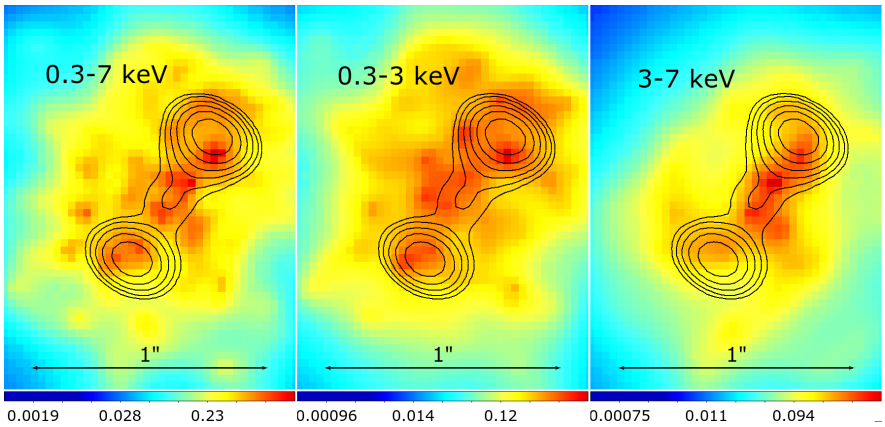

Figure 5. Chandra image of PKS 0023−26 in three energy bands overlaid with the radio continuum contours. The X-ray images were binned to 1/16th ACIS pixel size and adaptively smoothed with a Gaussian kernel (see details in the text). The 87 GHz radio continuum contours levels are (1, 2.3, 5.6, 11, 19, 33) mJy beam^{-1} (beam = $0\farcs163 \times 0\farcs09474$).

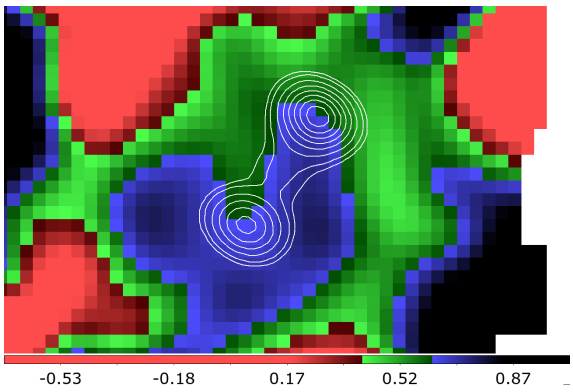

Figure 6. Color map of X-ray hardness ratio overlaid with the contours of the radio source. The hardness ratio is defined as HR = (H − S)/(H + S), where H = 2–7 keV and S = 0.3–2 keV. The color scale is shown at the bottom of the image, with the blue marking harder and the green/red softer X-rays.

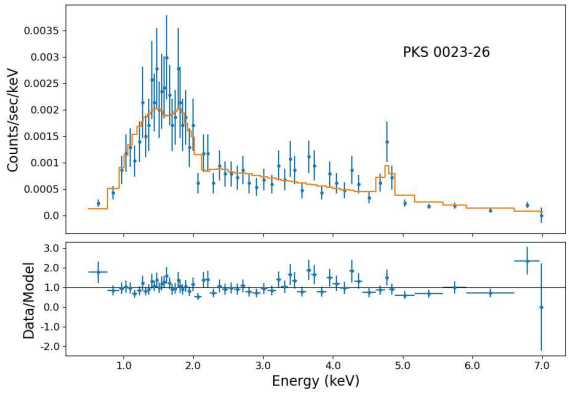

Figure 7. PKS 0023−26 X-ray spectra fit with an absorbed power-law model and addition of the Fe Kα emission line. The counts were grouped into 10 counts per bin for plotting. Top: the data (blue points) and the model (orange solid line). Bottom: the ratio of data to model.

two sectors and we only give upper limits. The Fe Kα emission line is strong in sectors 1, 2, and 4 with a relatively large equivalent width and located at consistent energies, but the line is quite weak in sector 3.

4. Discussion

We have presented the results from a deep Chandra observation of a powerful radio source, PKS 0023−26. We found an absorbed X-ray nucleus with the Fe Kα emission line, which signals the presence of a reflection medium within 7 kpc of the X-ray source region. Our high-angular-resolution X-ray image traces the distribution of hot gas, which is closely aligned with and extends beyond the radio source, especially in the direction perpendicular to the axis of the radio source (soft X-rays). We did not detect any diffuse X-ray emission outside a radius of ∼20 kpc and concluded that despite several galaxies being present at similar redshifts there is no rich X-ray cluster associated with PKS 0023−26. We placed a 90% limit of $L_{(0.5-2\ \mathrm{keV})} < 3.2 \times 10^{42}$ erg s^{-1} on the luminosity from a hot plasma with a temperature of $kT = 0.5$ keV, which is consistent with X-rays from a group of galaxies. In the following, we discuss our results in the context of an evolving radio jet and its impact on the ISM.

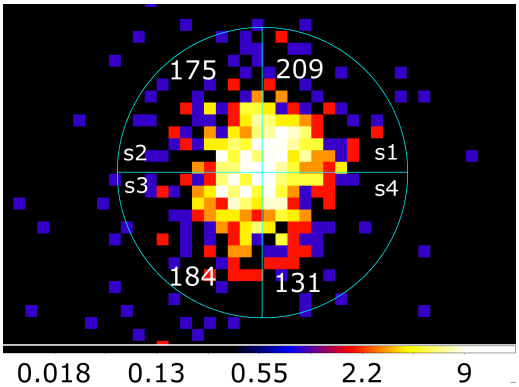

Figure 8. X-ray image showing the pie regions selected for spectral analysis. The numbers of counts in the 0.3–7 keV energy range are marked in the image; the sectors are labeled s1, s2, s3, and s4. The X-ray image is binned into 1/4th ACIS pixel size ($0\farcs123$) and the radius of the circle is equal to $1\farcs5$.

4.1. Large-scale Environment

Based on analysis of galaxy number counts, PKS 0023−26 appears to be located in a relatively rich environment, with a number of close companions seen in projection (C. Ramos Almeida et al. 2013). Three of these companions—all within a projected radial distance of 120 kpc of PKS 0023−26—have

Table 3
Best-fit X-Ray Model Parameters for the Sectors

Parameter	s1	s2	s3	s4
$N_H(z=0.322)$	5.2 (<7.0)	5.9 (<8.8)	<3.2	<2.5
Γ	$1.77^{+0.47}_{-0.43}$	$2.24^{+0.63}_{-0.52}$	$1.15^{+0.26}_{-0.23}$	1.20 ± 0.27
Norm	$3.8^{+2.9}_{-2.5}$	$4.7^{+4.9}_{-2.1}$	$2.1^{+0.7}_{-0.5}$	$1.67^{+0.56}_{-0.41}$
E(Fe Kα)	6.28 ± 0.12	$6.22^{+0.19}_{-0.21}$	6.4 ± 0.5	6.33 ± 0.08
EW	$0.450^{+0.374}_{-0.267}$	$0.742^{+0.662}_{-0.336}$	$0.204^{+0.174}_{-0.155}$	$0.735^{+0.119}_{-0.400}$

Note. Galactic absorption (phabs model) of $N_H = 1.82 \times 10^{20}$ cm^{-2} included in all models; $N_H(z)$—intrinsic absorption (zphabs model) is given in units of 10^{21} cm^{-2}; redshift $z = 0.322$ is frozen for the intrinsic absorption. The normalization of a power-law model is defined at 1 keV and given in units of 10^{-6} photons cm^{-2} s^{-1} keV^{-1}. Equivalent width is in keV units. Uncertainties are 90% except for EW with 1σ errors from simulations.

spectroscopic redshifts that are similar to PKS 0023−26 (C. Tadhunter et al. 2011: radial velocity differences of $+690 \pm 34$, $+200 \pm 75$, and $+280 \pm 60$ km s^{-1} relative to the rest frame of PKS 0023−26). However, our Chandra X-ray image shows that the emission is concentrated on PKS 0023−26 and a second object about 18″ away (i.e., ∼80 kpc) but does not show the X-ray diffuse component typically associated with clusters of galaxies. While the X-ray luminosity of the gas component in the central 1.″5 (∼7 kpc) is relatively large ($\sim 3 \times 10^{43}$ erg s^{-1}) the limit on gas luminosity in the surrounding 12″ (56.6 kpc) is much more modest (a few $\times 10^{42}$ erg s^{-1}).

Comparison with the X-ray luminosity profiles of other nearby systems confirms that if PKS 0023−26 were located at the center of even a poor galaxy cluster (e.g., AWM 4, E. O'Sullivan et al. 2010) or a rich, cool-core galaxy group (e.g., NGC 5044, E. O'Sullivan et al. 2017) the extended intracluster or intragroup medium (IGrM) would be visible in our Chandra spectrum of 1.″5–12″ radius. However, the IGrM of a less massive group could go undetected; systems with typical temperature ∼0.5 keV can have luminosities of only a few $\times 10^{41}$ erg s^{-1} within 50 kpc (S. F. Helsdon et al. 2005).

The distribution of the cold molecular gas observed by ALMA (R. Morganti et al. 2021; Paper I) suggests the presence of ongoing interaction between the host galaxy of PKS 0023−26 and surrounding galaxies, with tails of gas pointing in the direction of nearby (in projection) galaxies. The origin of the large amount of cold molecular medium is likely to be accretion from these companions. This is in contrast to cool-core clusters (e.g., B. R. McNamara et al. 2016; H. R. Russell et al. 2019). Cooling from the IGrM can be a source of molecular gas in the dominant ellipticals of galaxy groups with X-ray luminosities comparable to the upper limit on extended emission around PKS 0023−26 (E. O'Sullivan et al. 2018; V. Olivares et al. 2022). However, examples of tidal accretion of cold gas from neighbors become more common in lower-mass galaxy groups (e.g., in NGC 5903, NGC 315, and NGC 1587; P. N. Appleton et al. 1990; R. Morganti et al. 2009; V. Olivares et al. 2022), which is unsurprising since the group environment brings galaxies into close proximity at low relative velocities, and galaxies are much less likely to be ram-pressure-stripped than they would be in a rich cluster.

In central cluster galaxies the observed molecular gas structures seen around the radio bubbles (which contain radio jets) are explained as either a thin cover of clumpy molecular gas, expanding along with the growing radio bubbles, or molecular gas that is condensed in situ in the updrafts (e.g., B. R. McNamara et al. 2016; H. R. Russell et al. 2019). In PKS 0023−26 the former hypothesis appears more likely: what we are observing is the interaction between the expanding/growing radio lobes and the molecular gas accreted from companion galaxies.

Past studies of quasars indicated no differences between the environments of radio-quiet and radio-loud quasars, with only a few radio quasars found in X-ray-bright clusters. Recent studies of the environment of low-redshift radio galaxies and radio quasars using a low-frequency radio observation in the LOFAR Two-meter Sky Survey (LoTSS DR2; T. Pan et al. 2025) confirmed that luminous quasars are very rare in clusters, whereas a large fraction of less luminous radio galaxies are located in cluster centers. We find that PKS 0023−26 is in a group (not a strong cluster), which agrees with this statistical finding and also supports our findings about the origin of the molecular gas in PKS 0023−26.

4.2. Molecular Clouds Environment

In Paper I we use ALMA observations of several CO transitions to study the morphology, kinematics, and physical conditions of the molecular gas. On large scales, the CO distribution is uniform and appears quiescent with a few streams of molecular gas extending toward nearby galaxies. The conditions in the vicinity of the radio source are quite different. We found extreme physical conditions implied by a nondetection of the CO(1–0) gas in the radio core region, where the peak of the CO(3–2) gas distribution is located. As shown by Figure 5 this is also the region where the X-ray emission is most intense. P. R. Maloney et al. (1996) considered physical processes in X-ray-irradiated molecular gas and showed that X-ray ionization can lead to destruction of CO molecules. A lack of CO(1–0) line emission coincident with intense X-ray radiation fields has been reported previously (e.g., C. P. O'Dea et al. 1994 in X-ray clusters). In the galaxy ESO 428-G014, there is a lack of CO(2–1) emission in the nuclear region, where instead molecular gas emitting H_2 is abundant (C. Feruglio et al. 2020), leading to the suggestion by these authors that the X-ray photons may interfere with the production of CO(1–0). They suggested that CO may be excited to higher excitation levels up the CO ladder in this region, due to irradiation by the hard X-ray field and/or shocks. A similar effect was noticed in NGC 2110 (G. Fabbiano et al. 2019a), where X-ray emission was detected with Chandra to fill the CO(1–0) nuclear "lacuna" (D. J. Rosario et al. 2019). The lack of CO(1–0) emission in the nuclear region of PKS 0023−26, contrasted with the peak of X-ray emission in the same region, is consistent with these previous suggestions and theoretical predictions that the X-ray photons may excite CO to higher excitation levels in regions of intense X-ray photon fields. The close alignment between the molecular gas distribution, elevated CO excitation levels, and the radio axis further indicates that these intense X-ray fields likely result from interactions along the jet.

In ALMA data we also observed a large velocity dispersion of cold gas at the northern radio lobe, suggesting interactions between the expanding radio lobe and the molecular ISM, inducing turbulence (Paper I). Such interactions were also supported by the detection of high CO(3–2) to CO(2–1) line ratios, R_{32} (Figure 9). At the edge of the radio lobes, about

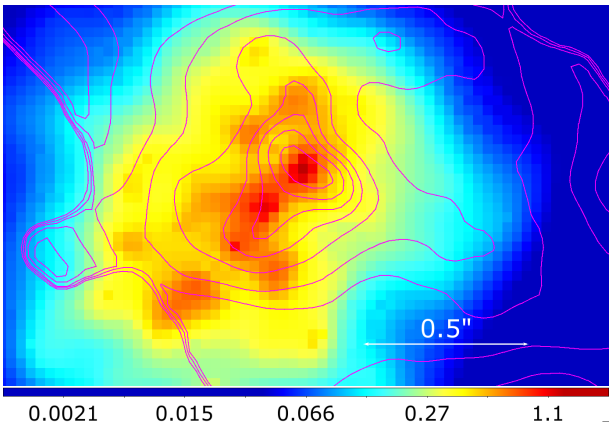

Figure 9. X-ray image (0.3–7 keV) overlaid with the contours of the CO(3–2)/CO(2–1) line ratio from the ALMA observations (Paper I). The X-ray image was adaptively smoothed as in Figure 5. The magenta contours are from the map of line ratio with the levels starting at the peak 1.05, 1.0, 0.95, 0.9, 0.82, 0.7, 0.6, 0.4, and 0.2.

$\sim$2 kpc from the core, the molecular gas traced by CO(2–1) and CO(3–2) appeared to wrap around the radio source, where the molecular gas was pushed aside or blocked from reaching the central regions. Furthermore, the CO(2–1) and CO(3–2) radiation appeared to be faint in the regions of the radio lobes. Interestingly, the map of CO(3–2) to CO(2–1) line ratio (Figure 9) indicates that the X-ray emission at the site of the northern lobe coincides with the region of the highest line ratio (dominated by the CO(3–2)), supporting the idea of the jet driving strong shocks through dense clouds, heating and destroying them, and producing thermal X-ray radiation.

The distribution and kinematics of the molecular gas at the end of the jet suggest that the interactions compress the ISM and increase its density, resulting in efficient cooling. Such interactions may perhaps explain the morphology of the molecular gas around the northern radio lobe. This point might also be supported by the map of X-ray hardness ratio (Figure 6), showing softer X-rays in the northern regions, similar to what was observed at the location of the jet–ISM interaction in another radio galaxy, NGC 1167/B20258+35 (G. Fabbiano et al. 2022).

4.3. Jet–ISM Interactions—Heating and the Cocoon

The distribution of CO line ratios outside the radio source, in particular in the region perpendicular to the jet direction, implies the presence of a cocoon of gas resulting from the jet–ISM interactions (Paper I). Our Chandra images show the X-ray emission elongated in the same direction as the radio emission, and enveloping it, suggesting jet heating (see Section 3.3) and supporting the presence of a cocoon of shocked gas. Therefore, we might expect that the X-rays are produced by strong interactions between the jet and the preexisting warm/cold gas: as the gas structures are shredded and heated by the jet-induced shocks, perhaps they could produce X-ray emission that is enhanced compared to that of the underlying X-ray halo (e.g., in 3C 171, M. J. Hardcastle et al. 2010; 3C 305, M. J. Hardcastle et al. 2012; PKS B2152-69, C. Ly et al. 2005; D. M. Worrall et al. 2012). If the preexisting warm/cool medium has fairly low densities (perhaps not too unlikely on kiloparsec scales) it may not be able to survive the shredding to cool to a molecular phase, hence explaining the hollowing out of the molecular gas at the sites of the lobes.

We can place some limits on the mass of hot gas in the cocoon based on its X-ray luminosity, but these depend on the volume assumed. If we assume a prolate ellipsoid cocoon closely coupled to the radio jets, then the X-ray image suggests that its length is $\sim 1\farcs13$ (5.4 kpc, along the jet axis) and width $\sim 1''$ (4.7 kpc). Subtracting the volume of the radio lobes (considered as 1.6 kpc diameter spheres), the X-ray emission would arise from a volume of $\sim$52.4 kpc^3, containing $\sim 3.8 \times 10^8\ M_\odot$ of hot gas. This is comparable within a factor of a few with the masses of hot gas found in the central few kiloparsecs of group-dominant galaxies (e.g., $10^8\ M_\odot$ in the central 2.4 kpc of NGC 777, E. O'Sullivan et al. 2024), so it is plausible that a significant fraction of the cocoon material may arise from a preexisting hot medium. However, we note that this mass estimate is relatively conservative, and will increase if the volume is larger than we have assumed; in the unlikely case that the hot gas fills the whole spectral extraction region of $1\farcs5$ radius the mass would be $\sim 2 \times 10^9\ M_\odot$, much less consistent with the masses of hot gas found in group cores. In either case, a contribution from shock-heated low-density cold gas may also be needed. We note that some of the mass of hot gas in the aligned structures might originate in the destruction of the cold molecular clouds by the interaction of the radio jets with the cool, merger-origin ISM in the central parts of the galaxy.

4.4. Nuclear Region

The results of the X-ray spectral analysis of PKS 0023−26 presented in Section 3.3 were based on the source area covering the central $<$7 kpc region of the host galaxy, which includes the radio source and molecular gas resolved by ALMA. We detect intrinsic absorption with an equivalent neutral hydrogen column density of $6.1^{+6.4}_{-5.2} \times 10^{21}\,\mathrm{cm}^{-2}$, a spectrum with a relatively hard photon index of $\Gamma = 1.45 \pm 0.25$ (uncertainties are 90%) and the Fe Kα emission line.

The Fe Kα emission line with EW $= 0.335^{+0.11}_{-0.06}$ keV could originate anywhere within this region. The fluorescence Fe Kα line is usually interpreted as a reflection of the cold medium in the inner few parsecs around a supermassive black hole. However, recent Chandra studies of several nearby galaxies found hard X-rays and Fe Kα emission on larger kiloparsec scales (e.g., G. Fabbiano et al. 2018; G. Fabbiano 2019; M. L. Jones et al. 2020, 2021). Our high-resolution image analysis shows slightly harder emission toward the southern radio lobe. The spectral modeling of the sectors shows differences in the equivalent width of the emission line, potentially indicating a preference for the reflection angles in the sectors perpendicular to the radio axis.

We measure the X-ray luminosity, corrected for absorption, of $L_{2-10\,\mathrm{keV}} = 3.1 \times 10^{43}\,\mathrm{erg\,cm^{-2}\,s^{-1}}$, which is in agreement with the earlier XMM-Newton measurements by B. Mingo et al. (2014). However, we note that the spectral energy range in the Chandra observation limits our determination of the intrinsic emission of the AGN, and additional hard X-ray data, at $>$10 keV, are needed to improve current constraints on luminosity and absorption.

4.5. Outflows

Multiband observations show different types of outflow present in PKS 0023−26. The high jet power (a few $\times$ 10^{46} erg s^{-1}) derived by R. Morganti et al. (2021) indicates that the radio source and the jet have enough energy on kiloparsec scales to accelerate and disperse the gas. Strong AGN radiation could also power the outflows (M. C. Begelman et al. 1983; C. M. Harrison et al. 2018). An outflow of ionized gas with a mass outflow rate in the range $0.13 < \dot{M} < 1.47\ M_\odot$ yr^{-1} was indicated by strong and broad (FWHM > 1000 km s^{-1}) optical emission lines (J. Holt et al. 2008; H.-Y. Shih et al. 2013; F. Santoro et al. 2020). The ionized outflow has a radial extent larger than the size of the radio source and exhibits high densities attributed to gas compression resulting from the jet–ISM interaction. However, the strong emission lines are attributed to AGN photoionization and not shocks associated with the interactions (see F. Santoro et al. 2020). The mass outflow rate of the cold molecular gas within the $\sim$1 kpc region observed with ALMA is $\dot{M} \lesssim 20\ M_\odot$ yr^{-1}. This is much higher than the outflow rate of the ionized gas component (F. Santoro et al. 2020), which agrees with the outflow rates observed in other sources.

X-rays could arise from AGN-photoionized gas or a shock-heated medium. Chandra studies of low-redshift radio and Seyfert galaxies where the soft X-ray spectra could be spatially resolved imply that a mixture of photoionized and shock-heated gas is present in these systems (e.g., J. Wang et al. 2011, D. Ł. Król, private communication). Chandra observations of powerful radio galaxies with aligned radio and X-ray morphology, and the spatial–spectral properties of hot gas point to the shock heating process (e.g., 3C 171, 3C 305; M. J. Hardcastle et al. 2010, 2012). In PKS 0023−26 the X-ray emission is closely aligned with the radio axis and has a similar extent to the radio source in the direction of the radio axis, which also argues for the shocks.

Measurement of the outflow rate of the hot gas in PKS 0023−26 is challenging due to the low signal in our data. Although we can estimate the upper limit of the outflow rate assuming that all the hot gas with a mass of $3.8 \times 10^8\ M_\odot$ (see Section 4.3) participates in the outflow, such a scenario is unlikely. Using $\dot{M} \sim M_{\rm out} \times v_{\rm out}/r_{\rm out}$, the same outflow velocity as the velocity of the ionized wind, $v_{\rm out} = 890$ km s^{-1} (F. Santoro et al. 2020), and the extent of $\sim$1 kpc, we get $\sim 350\ M_\odot$ yr^{-1}. This is a very high mass outflow rate in comparison to the rates typically observed in X-ray outflows (see, e.g., F. Fiore et al. 2017). On the other hand, the recent observation of a radio-quiet quasar, PDS 456, shows such high mass outflow rates with relativistic velocities of the clumpy wind (Xrism Collaboration et al. 2025).

We can calculate the sound speed in hot, uniformly distributed gas using the expression $c_s = \sqrt{\hat{\gamma} kT/\mu m_p}$, assuming nonrelativistic gas ($\hat{\gamma} = 5/3$) and the mean molecular weight of the gas $\mu = 0.6$. For a gas temperature of $kT = 0.9$ keV the measured sound speed is $\sim$500 km s^{-1}. Given the high velocity of the warm outflows ($\sim$1000 km s^{-1}), which exceeds the local sound speed, the presence of shocks is inevitable. If we assume that temperature $kT = 0.9$ keV is the postshock temperature then the expected shock velocity for fully ionized gas would be $v_{\rm shock} = \sqrt{16 kT/\mu m_p} \sim 870$ km s^{-1}, so relatively close to the velocity of the warm outflow. The Mach number for such a shock would be within $\mathcal{M} \sim 1.75 - 2$, so the shock would be in the supersonic regime with the gas compressed by a factor of $\sim$2. Although such shocks cannot be directly resolved in our X-ray data, our observations support the presence of a cocoon structure resulting from the interaction between the expanding radio source and the surrounding medium.

Similar and also stronger shocks driven by expansion of radio sources into the ISM have been resolved in other systems. For example, shocks with Mach numbers of $\sim$4 have been detected within $\sim$10 kpc in the radio galaxy NGC 3108 (J. H. Croston et al. 2007) and the Seyfert galaxy Markarian 6 (B. Mingo et al. 2011). Additionally, a weaker shock with a Mach number $<$2 has been observed at the site of a radio lobe approximately $\sim$20 kpc from the center of its galaxy (A. Siemiginowska et al. 2012).

Strong outflows are not commonly associated with galaxies in the centers of galaxy clusters. Furthermore, quasars residing within X-ray clusters are extremely rare, with only a few currently known (e.g., A. Siemiginowska et al. 2005, 2010; H. R. Russell et al. 2010). Therefore, a nondetection of strong X-ray emission typical of a galaxy cluster (see Section 4.1) is perhaps not surprising.

5. Summary and Conclusions

We have discussed the results of a deep Chandra X-ray observation of the young radio source PKS 0023−26 associated with a powerful quasar. The source is surrounded by cold molecular gas studied with ALMA. Several galaxies with similar redshift indicated the possibility that the diffuse X-ray emission from a cluster of galaxies can be observed in X-rays. We did not detect any diffuse X-ray emission at the luminosity expected from a typical X-ray cluster. We placed a limit on the X-ray luminosity of a few $\times$ 10^{42} erg s^{-1} within a region of $\sim$60 kpc located outside the central $r = 7$ kpc region. This limit does not rule out the possibility that PKS 0023−26 is located in a low-temperature poor galaxy group.

We observed the X-ray morphology of hot gas in the central region to be elongated and extended beyond the radio source in the direction perpendicular to the jet axis. The enhanced X-ray emission at the location of the northern lobe points to the site of jet–cloud interactions, resulting in shock heating of the gas. It is also the location of the peak of the CO(3–2)/CO(2–1) line emission, suggesting that the interactions between the jet and the cold medium result in the X-ray radiation that excites CO. The estimated Mach number of $\mathcal{M} = 1.75 - 2$ for the shock in PKS 0023−26 is in agreement with observations of shocks in other radio galaxies, pointing to the prevalent impact of jets on the ISM.

The X-ray spectrum of the central region ($r = 7$ kpc) shows a mildly absorbed AGN and an Fe Kα emission line at $E \sim 6.4$ keV, signaling a reflection from the cold gas. The observed equivalent width of the line is in agreement with a mildly absorbed AGN. However, the limited spectral energy coverage does not allow for detailed constraints on the intrinsic AGN spectrum and the amount of absorption. X-ray spectra at higher energy, such as provided by NuStar, are needed to better constrain these parameters in the future.

Acknowledgments

We thank the referee for comments and additional references that improved the manuscript. We thank Dominika Król for a discussion of the outflow ionization structure,

Beatrice Mingo for a discussion of the XMM data, and Kenny Glotfelty for helping with merging Chandra observations. Support for this work was provided by the National Aeronautics and Space Administration through Chandra Award Number GO1-22118X issued by the Chandra X-ray Observatory Center, which is operated by the Smithsonian Astrophysical Observatory for and on behalf of the National Aeronautics and Space Administration under contract NAS8-03060. A.S., G.F., E.O., and D.B. acknowledge support from NASA Contract NAS8-03060 to the Chandra X-ray Center.

This research has made use of data obtained from the Chandra Data Archive, and software provided by the Chandra X-ray Center (CXC) in the application packages CIAO and Sherpa. It employs a list of Chandra data sets, obtained by the Chandra X-ray Observatory, contained in the Chandra Data Collection (CDC) DOI:10.25574/cdc.400.

This paper makes use of the following ALMA data: ADS/JAO.ALMA#2022.1.01498.S. ALMA is a partnership of ESO (representing its member states), NSF (USA) and NINS (Japan), together with NRC (Canada), MOST and ASIAA (Taiwan), and KASI (Republic of Korea), in cooperation with the Republic of Chile. The Joint ALMA Observatory is operated by ESO, AUI/NRAO and NAOJ.

Appendix A
PKS 0023−26 X-Ray Data Analysis—Additional Figures

In this section we include additional figures presenting the results of X-ray data analysis. Figure 10 shows X-ray counts images for each single-epoch Chandra observation of PKS 0023-26 in the 0.3−7 keV energy range and a subpixel binning. Table 4 lists the Chandra observation id and the best-fit model parameters for each single-epoch spectrum and the resulting model flux.

Figures 11 and 12 present the parameter distributions from the MCMC sampling for 2D image model and the spectral model presented in Sections 3.2 and 3.3 respectively.

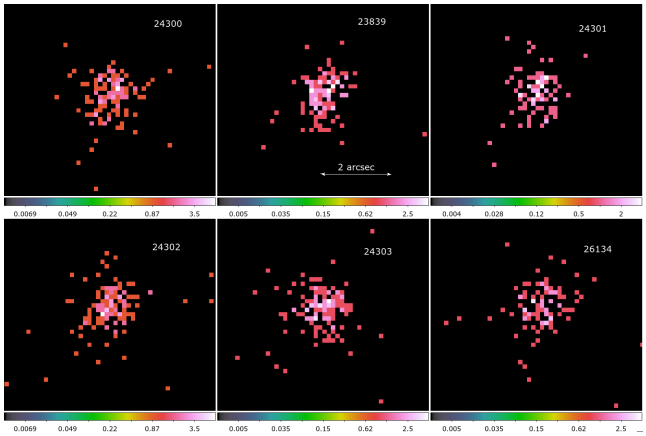

Figure 10. Chandra ACIS-S X-ray image of PKS 0023−26 in the 0.3–7 keV energy range. Each panel is $5\farcs2 \times 6\farcs0$ in size and displays a single observation with the obsid number marked in the upper right corner. The $2''$ scale bar is shown in the upper central panel. The pixel size is $0\farcs123$. The color indicates the number of counts per pixel and the color bar is shown at the bottom of each panel.

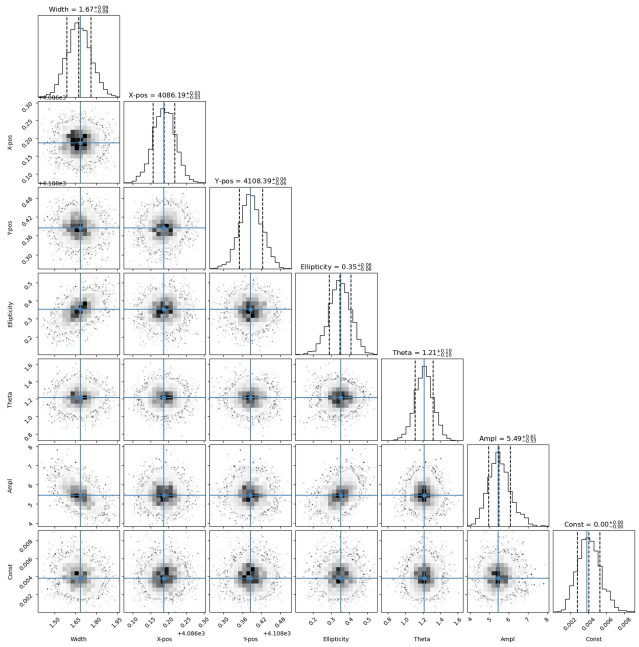

Figure 11. The parameter distributions for the 2D Gaussian model fit to the broad X-ray image of PKS 0023−26 obtained using `get_draw()`, the Bayesian MCMC sampling in Sherpa. Model expression as defined in the Sherpa fit: `psf(gauss2d+const2d)`. The best-fit model parameters are listed above relevant histograms and are marked by blue vertical lines; the mean and 1σ range for the distribution are marked by dashed vertical lines. The corner plot was made using `corner` Python package (D. Foreman-Mackey 2016).

Table 4
Model Parameters for Single-epoch Observations

Date	Obsid[a]	Photon Index	Norm[b]	$f_{0.5-7.0\ \mathrm{keV}}$[c]	Cstat/dof
2021-09-13	24302	$1.3^{+0.34}_{-0.28}$	$10.0^{+4.9}_{-2.5}$	$7.6^{+3.5}_{-0.3}$	305.8/444
2021-09-19	24301	$0.94^{+0.31}_{-0.32}$	$8.7^{+3.4}_{-2.6}$	$9.5^{+6.5}_{-3.8}$	296.4/444
2021-09-20	23839	$0.97^{+0.27}_{-0.27}$	$8.7^{+2.8}_{-2.3}$	$9.4^{+5.3}_{-3.7}$	330.0/444
2021-09-21	26134	$1.16^{+0.32}_{-0.32}$	$6.5^{+2.4}_{-1.8}$	$5.4^{+3.9}_{-2.1}$	298.8/444
2021-09-23	24300	$1.25^{+0.28}_{-0.28}$	$8.3^{+2.5}_{-2.1}$	$6.4^{+3.3}_{-2.3}$	289.8/444
2021-09-24	24303	$1.69^{+0.28}_{-0.28}$	$13.2^{+3.6}_{-3.1}$	$6.9^{+2.6}_{-2.3}$	292.2/444

Notes. Galactic absorption (`phabs` model) of $N_{\mathrm{H}} = 1.82 \times 10^{20}\ \mathrm{cm}^{-2}$ was included in all fitting with a power-law model.
[a] Chandra obsid.
[b] Norm—normalization of a power law is defined at 1 keV in units of 10^{-5} photons $\mathrm{s}^{-1}\ \mathrm{cm}^{-2}\ \mathrm{keV}^{-1}$.
[c] Flux in the 0.5–7 keV energy range in units of 10^{-14} erg $\mathrm{s}^{-1}\ \mathrm{cm}^{-2}$; uncertainties are 90%.

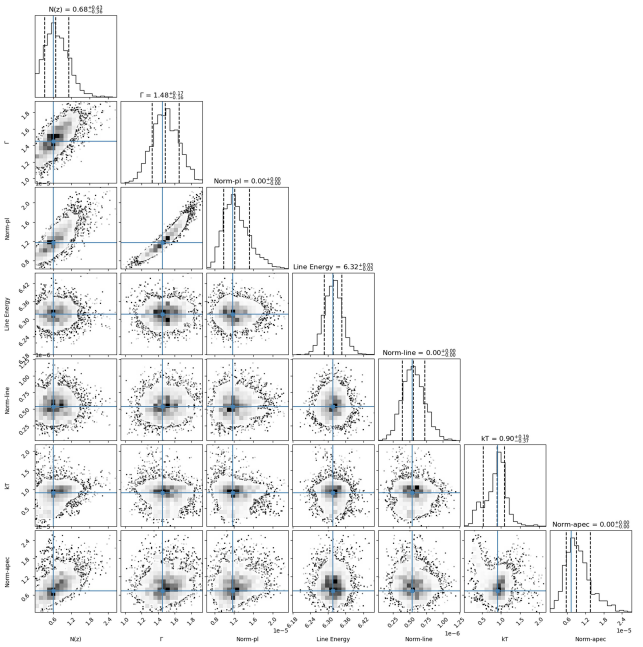

Figure 12. Distributions of the model parameters for spectral model fit to PKS 0023−26 `phabs*zphabs*(powlaw1d+zgauss)+phabs*apec` from the Metropolis–Hastings sampling with `get_draws` in Sherpa. The labels show parameters on each axis. The best-fit values from the fit are marked by the solid blue square and lines, while the distribution quantiles are marked by dashed lines, the central dashed line shows the mean. The top of each column shows the mean of the parameter value and 1σ quantiles.

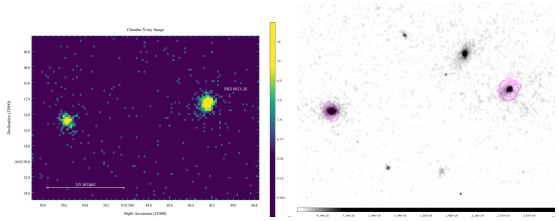

Figure 13. Left: Chandra ACIS-S image in the 0.3–7 keV energy range binned to half of the ACIS pixel size of 0.″246. Two X-ray sources are separated by about 18″. The scale is logarithmic with the color bars indicating counts per pixel. Right: optical image from Gemini overplotted with the X-ray contours. The X-rays are associated with PKS 0023−26 and the second source to the east of it.

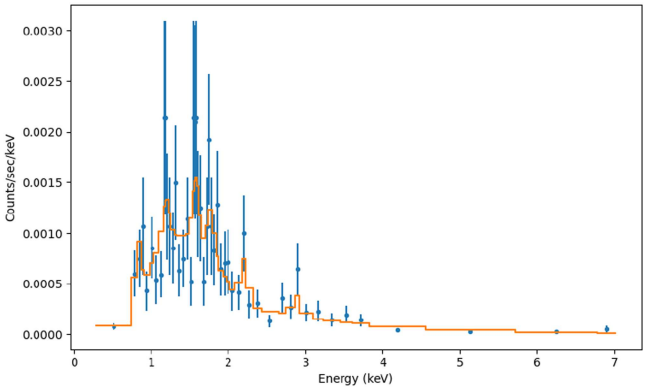

Figure 14. X-ray spectrum (blue points) of the second source overplotted with the best-fit model (solid orange line). The spectrum was grouped by 5 counts per bin for the visualization.

Appendix B
X-Ray Properties of the Second X-Ray Source

Figure 13 shows an optical image from Gemini GMOS-S (C. Ramos Almeida et al. 2011) overplotted with the X-ray contours from the Chandra observation. In addition to the PKS 0023−26 X-ray source we also detect a second X-ray source located about 18″ to the east. The source is present in the Gaia DR2 (Gaia Collaboration et al. 2018) optical catalog with ID = 2323489174407213824 and an average G magnitude of 20.6525 ± 0.0211. This Gaia source is fainter than PKS 0023−26 in X-rays and it was not separated in the XMM-Newton analysis presented by B. Mingo et al. (2014), who used a 30″ extraction region for PKS 0023−26 analysis. We used the `specextract` tool to extract the X-ray spectra from each `obsid` assuming a circular region centered on this source with radius of 1.″5. These spectra were combined with `combined_spectra` to generate one spectrum that we fit using Sherpa. The total number of source net counts in the combined spectrum was 277.2 ± 16.8 (background counts $= 3.8 \pm 1.9$). We fit the spectrum with a power-law model, and because the residuals were quite large, we added several Gaussian lines to the model to obtain the best fit. Figure 14 shows the best-fit model overplotted on the X-ray spectrum and Table 5 presents the model parameters. We list the lines at the observed energy. The source does not have any redshift information in the literature; several galaxies in the field have a redshift consistent with PKS 0023−26 so we also assumed a redshift of 0.322 for the emission lines. We note that the power-law continuum with measured photon index of $2.33^{+0.19}_{-0.28}$ is steeper than the X-ray photon index of PKS 0023−26. We measure the soft-band X-ray flux of $f^{\rm cont}_{(0.5-2\,{\rm keV})} = 1.50^{+0.16}_{-0.18} \times 10^{-14}$ erg cm^{-2} s^{-1} for the continuum power law only and $f^{\rm full}_{(0.5-2\,{\rm keV})} = 1.81^{+0.21}_{-0.22} \times 10^{-14}$ erg cm^{-2} s^{-1} for the continuum plus emission line model. The hard-band flux for the power-law continuum is equal to $f^{\rm cont}_{(2-10\,{\rm keV})} = 1.04^{+0.24}_{-0.17} \times 10^{-14}$ erg cm^{-2} s^{-1}.

Table 5
Properties of the Emission Lines in the Second X-Ray Source

	E_{obs} (keV)	EW (keV)	ID (obs)	E_{rest} (keV)	ID (rest)
Line 1	0.82 ± 0.05	$0.198^{+0.101}_{-0.191}$	Fe XVII	1.084	Fe XXII
Line 2	1.58 ± 0.03	$0.124^{+0.060}_{-0.027}$	Mg XI	2.088	Si XIV
Line 3	$1.19^{+0.78}_{-0.08}$	$0.058^{+0.028}_{-0.042}$	Fe XXIV	1.57	Mg XI
Line 4	$2.89^{+0.09}_{---}$	$0.120^{+0.130}_{-0.00}$	S XV	3.82	Ca XIX
Line 5	$2.20^{0.04}_{-0.05}$	$0.241^{+0.068}_{-0.078}$	Si XIII	2.91	S XV
Line 6	$1.76^{0.12}_{-0.05}$	$0.075^{+0.098}_{-0.014}$	Mg XII	2.33	Si XIV
Power law	$\Gamma = 2.33^{+0.19}_{-0.28}$	Norm $= 6.63^{+0.61}_{-2.65}$	…	…	…

Note. Galactic absorption (phabs model) of $N_H = 1.82 \times 10^{20}$ cm^{-2} is frozen in the fit; redshift $z = 0.322$. The normalization of a power law model is defined at 1 keV and given in units of 10^{-6} photons cm^{-2} s^{-1} keV^{-1}. Equivalent width is in keV units with 1σ errors; power-law parameters are given in the last row with 90% uncertainties.

ORCID iDs

A. Siemiginowska https://orcid.org/0000-0002-0905-7375
R. Morganti https://orcid.org/0000-0002-9482-6844
G. Fabbiano https://orcid.org/0000-0002-3554-3318
E. O'Sullivan https://orcid.org/0000-0002-5671-6900
T. Oosterloo https://orcid.org/0000-0002-0616-6971
C. Tadhunter https://orcid.org/0000-0002-2951-3278
D. Burke https://orcid.org/0000-0003-4428-7835

References

Anders, E., & Grevesse, N. 1989, GeCoA, 53, 197
Appleton, P. N., Pedlar, A., & Wilkinson, A. 1990, ApJ, 357, 426
Begelman, M. C., McKee, C. F., & Shields, G. A. 1983, ApJ, 271, 70
Cielo, S., Bieri, R., Volonteri, M., Wagner, A. Y., & Dubois, Y. 2018, MNRAS, 477, 1336
Costa-Souza, J. H., Riffel, R. A., Souza-Oliveira, G. L., et al. 2024, ApJ, 974, 127
Cresci, G., Tozzi, G., Perna, M., et al. 2023, A&A, 672, A128
Croston, J. H., Kraft, R. P., & Hardcastle, M. J. 2007, ApJ, 660, 191
Di Matteo, T., Springel, V., & Hernquist, L. 2005, Natur, 433, 604
Eckmiller, H. J., Hudson, D. S., & Reiprich, T. H. 2011, A&A, 535, A105
Emonts, B. H. C., Morganti, R., Tadhunter, C. N., et al. 2005, MNRAS, 362, 931
Fabbiano, G. 2019, in The Chandra X-Ray Observatory, ed. B. Wilkes & W. Tucker (Bristol: IOP Publishing), 7
Fabbiano, G., & Elvis, M. 2022, in Handbook of X-Ray and Gamma-Ray Astrophysics, ed. C. Bambi & A. Sangangelo (Berlin: Springer), 92
Fabbiano, G., Paggi, A., & Elvis, M. 2019a, ApJL, 876, L18
Fabbiano, G., Paggi, A., Karovska, M., et al. 2018, ApJ, 865, 83
Fabbiano, G., Paggi, A., Morganti, R., et al. 2022, ApJ, 938, 105
Fabbiano, G., Siemiginowska, A., Paggi, A., et al. 2019b, ApJ, 870, 69
Fabian, A. C. 2012, ARA&A, 50, 455
Feruglio, C., Fabbiano, G., Bischetti, M., et al. 2020, ApJ, 890, 29
Fiore, F., Feruglio, C., Shankar, F., et al. 2017, A&A, 601, A143
Foreman-Mackey, D. 2016, JOSS, 1, 24
Foster, A. R., Ji, L., Smith, R. K., & Brickhouse, N. S. 2012, ApJ, 756, 128
Freeman, P., Doe, S., & Siemiginowska, A. 2001, Proc. SPIE, 4477, 76
Fruscione, A., McDowell, J. C., Allen, G. E., et al. 2006, Proc. SPIE, 6270, 62701V
Fukazawa, Y., Hiragi, K., Mizuno, M., et al. 2011, ApJ, 727, 19
Gaia Collaboration, Brown, A. G. A., Vallenari, A., et al. 2018, A&A, 616, A1
Guillard, P., Ogle, P. M., Emonts, B. H. C., et al. 2012, ApJ, 747, 95
Hardcastle, M. J., Massaro, F., & Harris, D. E. 2010, MNRAS, 401, 2697
Hardcastle, M. J., Massaro, F., Harris, D. E., et al. 2012, MNRAS, 424, 1774
Harrison, C. M., Costa, T., Tadhunter, C. N., et al. 2018, NatAs, 2, 198
Helsdon, S. F., Ponman, T. J., & Mulchaey, J. S. 2005, ApJ, 618, 679
Hickox, R. C., & Alexander, D. M. 2018, ARA&A, 56, 625
Hinshaw, G., Larson, D., Komatsu, E., et al. 2013, ApJS, 208, 19
Holt, J., Tadhunter, C. N., & Morganti, R. 2003, MNRAS, 342, 227
Holt, J., Tadhunter, C. N., & Morganti, R. 2008, MNRAS, 387, 639
Hopkins, P. F., Torrey, P., Faucher-Giguère, C.-A., Quataert, E., & Murray, N. 2016, MNRAS, 458, 816
Jarvis, M. E., Harrison, C. M., Thomson, A. P., et al. 2019, MNRAS, 485, 2710
Jones, M. L., Fabbiano, G., Elvis, M., et al. 2020, ApJ, 891, 133
Jones, M. L., Parker, K., Fabbiano, G., et al. 2021, ApJ, 910, 19
Król, D. Ł., Sobolewska, M., Stawarz, Ł., et al. 2024, ApJ, 966, 201
Kunert-Bajraszewska, M., Labiano, A., Siemiginowska, A., & Guainazzi, M. 2014, MNRAS, 437, 3063
Kunert-Bajraszewska, M., Siemiginowska, A., & Labiano, A. 2013, ApJL, 772, L7
Li, J., Kastner, J. H., Prigozhin, G. Y., et al. 2004, ApJ, 610, 1204
Lotz, J. M., Jonsson, P., Cox, T. J., et al. 2011, ApJ, 742, 103
Ly, C., De Young, D. S., & Bechtold, J. 2005, ApJ, 618, 609
Ma, J., Elvis, M., Fabbiano, G., et al. 2023, ApJ, 948, 61
Mahony, E. K., Oonk, J. B. R., Morganti, R., et al. 2016, MNRAS, 455, 2453
Maksym, W. P., Schmidt, J., Keel, W. C., et al. 2020, ApJL, 902, L18
Maloney, P. R., Hollenbach, D. J., & Tielens, A. G. G. M. 1996, ApJ, 466, 561
Massaro, F., Chiaberge, M., Grandi, P., et al. 2009, ApJL, 692, L123
Massaro, F., Harris, D. E., Liuzzo, E., et al. 2015, ApJS, 220, 5
Massaro, F., Harris, D. E., Tremblay, G. R., et al. 2010, ApJ, 714, 589
McNamara, B. R., & Nulsen, P. E. J. 2012, NJPh, 14, 055023
McNamara, B. R., Russell, H. R., Nulsen, P. E. J., et al. 2016, ApJ, 830, 79
Mingo, B., Hardcastle, M. J., Croston, J. H., et al. 2014, MNRAS, 440, 269
Mingo, B., Hardcastle, M. J., Croston, J. H., et al. 2011, ApJ, 731, 21
Morganti, R., & Oosterloo, T. 2018, A&ARv, 26, 4
Morganti, R., Oosterloo, T., Oonk, J. B. R., Frieswijk, W., & Tadhunter, C. 2015, A&A, 580, A1
Morganti, R., Oosterloo, T., Tadhunter, C., Bernhard, E. P., & Oonk, J. B. R. 2021, A&A, 656, A55
Morganti, R., Peck, A. B., Oosterloo, T. A., et al. 2009, A&A, 505, 559
Mukherjee, D., Bicknell, G. V., Sutherland, R., & Wagner, A. 2016, MNRAS, 461, 967
Mukherjee, D., Bicknell, G. V., Wagner, A. Y., Sutherland, R. S., & Silk, J. 2018, MNRAS, 479, 5544
Nesvadba, N. P. H., Lehnert, M. D., Eisenhauer, F., et al. 2006, ApJ, 650, 693
O'Dea, C. P. 1998, PASP, 110, 493
O'Dea, C. P., Baum, S. A., Maloney, P. R., Tacconi, L. J., & Sparks, W. B. 1994, ApJ, 422, 467
O'Dea, C. P., Mu, B., Worrall, D. M., et al. 2006, ApJ, 653, 1115
O'Dea, C. P., & Saikia, D. J. 2021, A&ARv, 29, 3
O'Dea, C. P., Worrall, D. M., & Tremblay, G. R. 2017, ApJ, 851, 87
Olivares, V., Salomé, P., Hamer, S. L., et al. 2022, A&A, 666, A94
Oosterloo, T., Morganti, R., Tadhunter, C., et al. 2025, A&A, 700, A22
O'Sullivan, E., Combes, F., Salomé, P., et al. 2018, A&A, 618, A126
O'Sullivan, E., Giacintucci, S., David, L. P., Vrtilek, J. M., & Raychaudhury, S. 2010, MNRAS, 407, 321
O'Sullivan, E., Kunert-Bajraszewska, E., Siemiginowska, A., et al. 2021, ApJ, 913, 105
O'Sullivan, E., Ponman, T. J., Kolokythas, K., et al. 2017, MNRAS, 472, 1482
O'Sullivan, E., Rajpurohit, K., Schellenberger, G., et al. 2024, ApJ, 970, 65
Paggi, A., Wang, J., Fabbiano, G., Elvis, M., & Karovska, M. 2012, ApJ, 756, 39
Pan, T., Fu, Y., Rottgering, H. J. A., et al. 2025, A&A, 695, A69
Pierce, J. C. S., Tadhunter, C. N., Gordon, Y., et al. 2022, MNRAS, 510, 1163

Protassov, R., van Dyk, D. A., Connors, A., Kashyap, V. L., & Siemiginowska, A. 2002, ApJ, 571, 545
Ramos Almeida, C., Bessiere, P. S., Tadhunter, C. N., et al. 2013, MNRAS, 436, 997
Ramos Almeida, C., Tadhunter, C. N., Inskip, K. J., et al. 2011, MNRAS, 410, 1550
Rosario, D. J., Togi, A., Burtscher, L., et al. 2019, ApJL, 875, L8
Ruffa, I., & Davis, T. A. 2024, Galax, 12, 36
Russell, H. R., Fabian, A. C., Sanders, J. S., et al. 2010, MNRAS, 402, 1561
Russell, H. R., McNamara, B. R., Fabian, A. C., et al. 2019, MNRAS, 490, 3025
Sabater, J., Best, P. N., Hardcastle, M. J., et al. 2019, A&A, 622, A17
Santoro, F., Tadhunter, C., Baron, D., Morganti, R., & Holt, J. 2020, A&A, 644, A54
Shih, H.-Y., Stockton, A., & Kewley, L. 2013, ApJ, 772, 138
Siemiginowska, A., Burke, D., Günther, H. M., et al. 2024, ApJS, 274, 43
Siemiginowska, A., Burke, D. J., Aldcroft, T. L., et al. 2010, ApJ, 722, 102
Siemiginowska, A., Cheung, C. C., LaMassa, S., et al. 2005, ApJ, 632, 110
Siemiginowska, A., LaMassa, S., Aldcroft, T. L., Bechtold, J., & Elvis, M. 2008, ApJ, 684, 811
Siemiginowska, A., Stawarz, Ł., Cheung, C. C., et al. 2012, ApJ, 750, 124
Sobolewska, M., Siemiginowska, A., Guainazzi, M., et al. 2019, ApJ, 871, 71
Stawarz, Ł., Ostorero, L., Begelman, M. C., et al. 2008, ApJ, 680, 911
Tadhunter, C., Holt, J., González Delgado, R., et al. 2011, MNRAS, 412, 960
Tadhunter, C., Morganti, R., Rose, M., Oonk, J. B. R., & Oosterloo, T. 2014, Natur, 511, 440
Tadhunter, C. N. 1991, MNRAS, 251, 46P
Travascio, A., Fabbiano, G., Paggi, A., et al. 2021, ApJ, 921, 129
Tzioumis, A., King, E., Morganti, R., et al. 2002, A&A, 392, 841
Ubertosi, F., Gitti, M., Brighenti, F., et al. 2023, A&A, 673, A52
Wang, J., Fabbiano, G., Risaliti, G., et al. 2011, ApJ, 729, 75
Worrall, D. M., Birkinshaw, M., Young, A. J., et al. 2012, MNRAS, 424, 1346
Xrism Collaboration, Audard, M., Awaki, H., et al. 2025, Natur, 641, 1132